

Relationship between the Annealing Temperature and the Presence of PbI_2 Platelets at the Surfaces of Slot-Die-Coated Triple-Halide Perovskite Thin Films

Dan R. Wargulski,* Ke Xu, Hannes Hempel, Marion A. Flatken, Steve Albrecht, and Daniel Abou-Ras*



Cite This: *ACS Appl. Mater. Interfaces* 2023, 15, 41516–41524



Read Online

ACCESS |

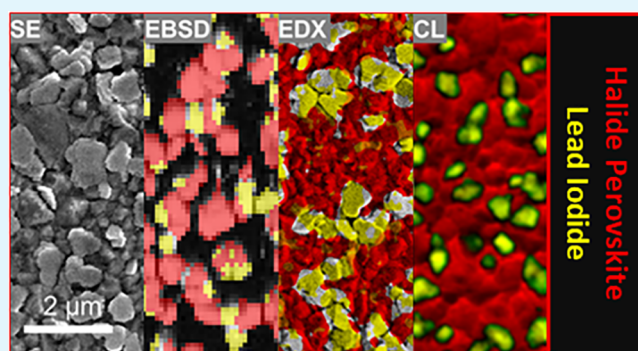
Metrics & More

Article Recommendations

Supporting Information

ABSTRACT: We investigated triple-halide perovskite (THP) absorber layers with 5 mol % MAPbCl_3 added to the double-halide perovskite $(\text{Cs}_{0.22}\text{FA}_{0.78})\text{Pb}(\text{I}_{0.85}\text{Br}_{0.15})_3$. As a deposition method, a highly scalable printing technique, slot-die coating, with a subsequent annealing step was used. We found a strong power conversion efficiency (PCE) dependence of the corresponding solar cells on the annealing temperature. The device performance deteriorated when increasing the annealing temperature from 125 to 170 °C, mainly via losses in the open-circuit voltage (V_{oc}) and in the fill factor (FF). To understand the mechanisms behind this performance loss, extensive characterizations were performed on both, the THP thin films and the completed solar-cell stacks, as a function of annealing temperature. Correlative scanning electron microscopy analyses, i.e., electron backscatter diffraction, energy-dispersive X-ray spectroscopy, and cathodoluminescence, in addition to X-ray diffraction and photoluminescence, confirmed the presence of PbI_2 platelets on the surface of the THP thin films. Moreover, the area fraction of the PbI_2 platelets on the film surface increased with increasing annealing temperature. The deteriorated device performance when the annealing temperature is increased from 125 to 170 °C is explained by the increased series resistance and increased interface recombination caused by the PbI_2 platelets, leading to decreased V_{oc} and FF values of the solar-cell devices. Thus, the correlative analyses provided insight into microscopic origins of the efficiency losses.

KEYWORDS: halide perovskites, hybrid photovoltaics, scanning electron microscopy, cathodoluminescence, slot-die coating, lead iodide



INTRODUCTION

Triple-halide perovskites (THPs)¹ are applied as top-cell absorber layers in perovskite-silicon tandem solar cells (PSTSCs). Developed as a wide-band-gap semiconductor,² it can reach the optimum band-gap energy for PSTSC top cells of about 1.7 eV³ without the efficiency-limiting, light-induced effect of halide phase segregation.^{4,5}

Recently, a record power conversion efficiency (PCE) for PSTSCs of 33.7% was achieved.⁶ However, this record was realized by solar cells fabricated on small device areas via laboratory-scale processes, such as spin-coating. While this technique has shown to be an excellent method to fabricate solar cells on about 1-cm²-large substrates, it is rather unsuitable for upscaling, i.e., for the transfer to industrial processes for solar modules. Printing techniques such as slot-die coating can be regarded as promising candidates for the industrial deposition of halide perovskites.

A previous work by Xu et al.⁷ investigated the effect of different annealing temperatures on slot-die-coated THP thin films and solar cells. The aim was to find optimal process parameters and to achieve a suitable crystallization of THP thin films without the application of antisolvents. Therefore,

N_2 quenching was used to dry the deposited ink, followed by an annealing step at various temperatures. It revealed an increasing amount of PbI_2 with increasing annealing temperatures detected by X-ray diffraction (XRD); however, these PbI_2 agglomerates were not further investigated, and their impact on the device performance is not discussed in detail.

Therefore, in the present contribution, we continue the work of Xu et al.⁷ by analyzing a series of THP thin films, annealed at temperatures ranging from 100 to 170 °C. Furthermore, completed solar cells from these stacks were investigated. Using various characterization methods in scanning electron microscopy (SEM) in addition to XRD and photoluminescence (PL), it was possible to identify the PbI_2 precipitates as homogeneously distributed secondary phases and to verify

Received: May 29, 2023

Accepted: August 16, 2023

Published: August 25, 2023



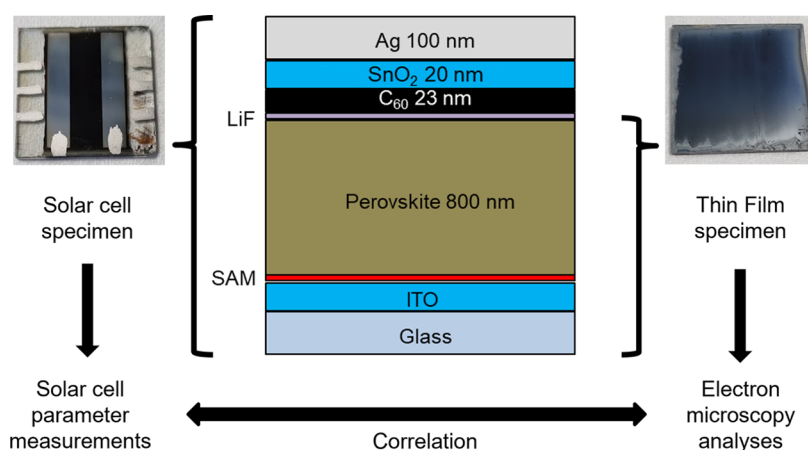


Figure 1. Schematic of the THP solar-cell structure and images of the THP solar-cell specimen made for determination of the solar-cell parameters and the THP thin-film specimen with an open THP surface for electron microscopy analyses.

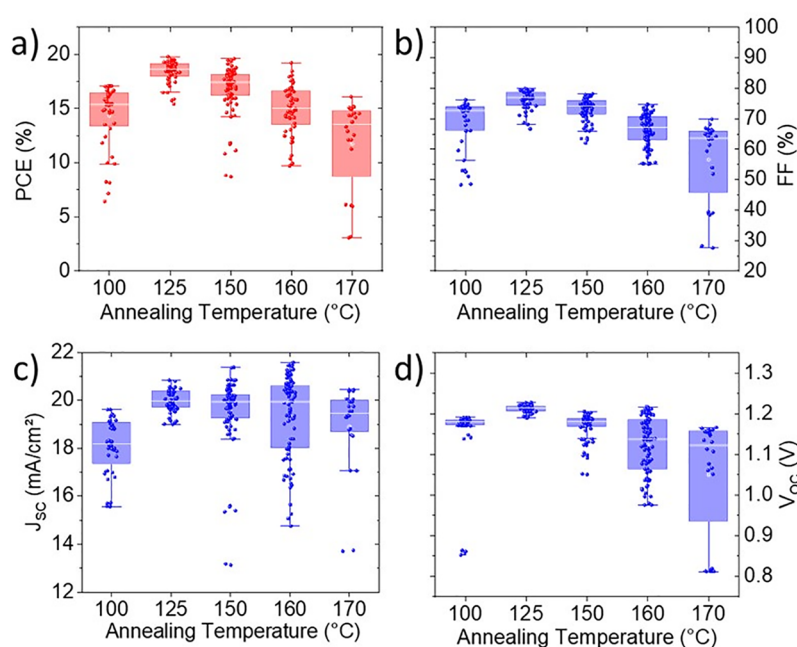


Figure 2. Photovoltaic parameters of the solar cells analyzed in the present work: (a) PCE, (b) FF, (c) J_{sc} , and (d) V_{oc} of solar cells annealed at temperatures between 100 and 170 °C. For PCE, FF, and V_{oc} , the median values exhibit local maxima at 125 °C annealing temperature and a decrease for higher temperatures.

that, indeed, PbI_2 forms platelets at the THP thin-film surface only. This detailed microscopic insight provided the possibility of proposing a specific model of how the PbI_2 precipitates affect the photovoltaic parameters of THP solar cells.

EXPERIMENTAL SECTION

Material Synthesis and Device Fabrication. The THP composition studied in the present work was 5 mol % $MAPbCl_3$ alloyed to a double-halide perovskite of stoichiometry $(Cs_{0.22}FA_{0.78})-Pb(I_{0.85}Br_{0.15})_3$. The THP deposition process consisted of slot-die coating and subsequently N_2 quenching by a N_2 knife for controlling thin-film drying, which acts as a replacement of the widely applied antisolvent dripping. The N_2 quenching followed an annealing step at temperatures of 100, 125, 150, 160, and 170 °C for 20 min.

The THP thin films in the THP/self-assembled monolayer (SAM)/indium–tin oxide (ITO)/glass and Ag/ SnO_2 / C_{60} /LiF/THP/SAM/ITO/glass stacks were prepared via very similar processes. For complete solar-cell stacks, LiF and C_{60} were thermally evaporated followed by the deposition of SnO_2 . The Ag back-contact

was deposited by thermal evaporation. The overall structures of both sample types are depicted in Figure 1. Further details about the materials synthesis, ink preparation, and thin-film deposition are given in the Supporting Information and by Xu et al.⁷

Solar-Cell and Thin-Film Characterization. The secondary electron (SE) images and cathodoluminescence (CL) mappings were acquired with a Zeiss Merlin scanning electron microscope at an acceleration voltage of 5 kV. The beam current was limited to 50–100 pA to reduce the electron-beam damage of the THP thin films, which can be detected well by reduced luminescence signals. The pixel size of the CL images was set to 27 nm, and the CL intensity was measured with a photomultiplier tube (300 μ m dwell time and 1 V gain). In order to obtain monochromatic CL images, 700 \pm 50 and 500 \pm 50 nm band-pass filters were applied. It was not possible to acquire hyperspectral images by the charge-coupled device due to the rapidly progressing beam damage and the necessarily longer integration time in this measurement mode.

The electron backscatter diffractometry (EBSD) and energy-dispersive X-ray spectroscopy (EDX) measurements were performed by using a Zeiss Ultra Plus scanning electron microscope equipped

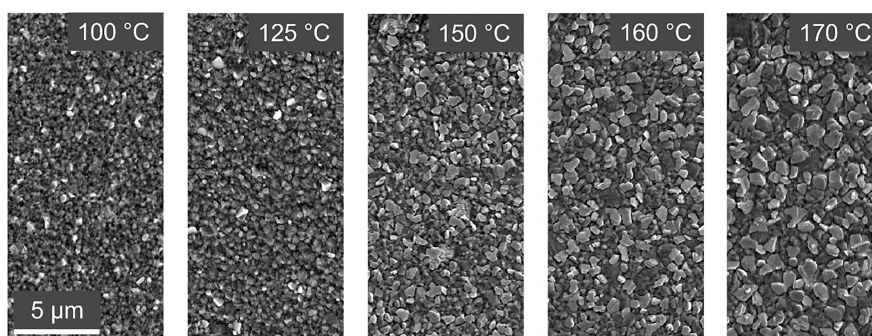


Figure 3. SE images of samples annealed at 100–170 °C showing contiguous THP thin films with increasing crystallite sizes for increasing temperature.

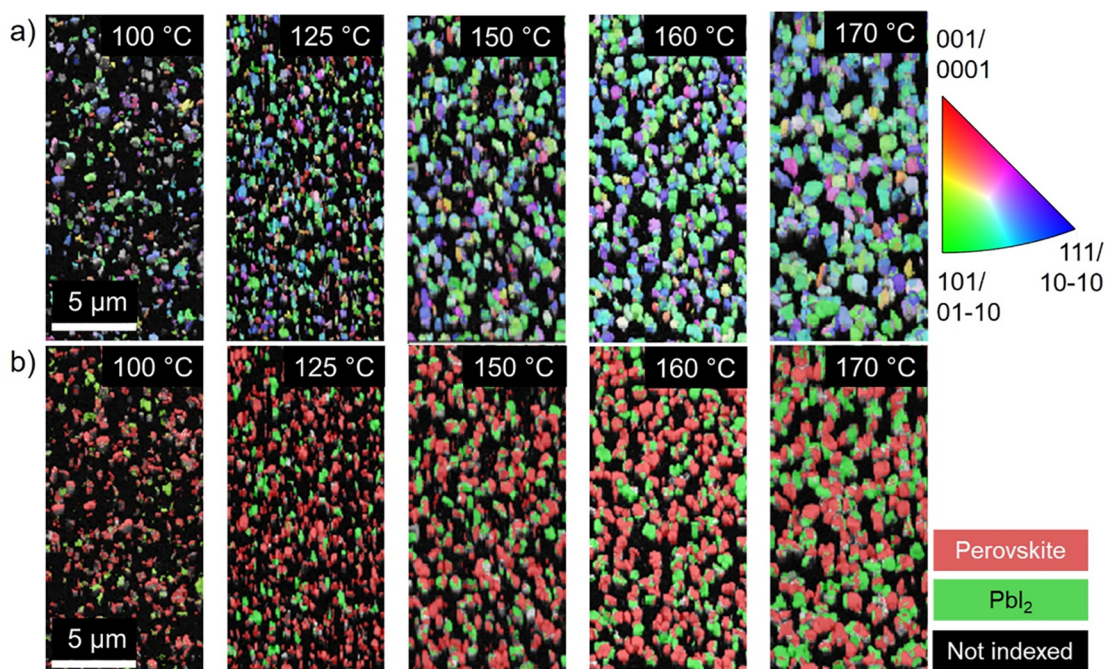


Figure 4. EBSD analyses with (a) the orientation–distribution maps (given by false colors; see the legend with orientations for the pseudocubic THP/trigonal PbI_2 phases) and (b) the phase distribution maps of the identified THP and PbI_2 phases.

with Oxford Instruments Symmetry EBSD and Ultim Extreme EDX detectors. The EBSD measurements were conducted at an acceleration voltage of 15 kV. The samples were tilted to an angle of 70° during the measurements. The step size was 50 nm. EDX spectra and elemental distribution maps were acquired at 3.5 kV on nontilted samples.

The solar cells with an active area of about 0.16 cm² were characterized in a sun simulator under 1-sun illumination through the glass substrate. The previous study of Xu et al.⁷ already reported about XRD and PL measurements, which are used and extended in the present work for further analyses and discussion (included in the Supporting Information).

RESULTS AND DISCUSSION

Analyses of THP Solar Cells. J – V characteristics of 258 solar cells in total were acquired, and the corresponding solar-cell parameters, i.e., the photoconversion efficiency (PCE), fill factor (FF), short-circuit current density (J_{sc}), and open-circuit voltage (V_{oc}), were determined. The data of the 100, 150, and 170 °C samples were extracted from the work by Xu et al.⁷ and added to those of the 125 and 160 °C samples measured for the present study.

In the previous study by Xu et al.,⁷ the solar cell with the THP film annealed at 150 °C performed the best. However, as shown in Figure 2, it was found in the present work that the maximum PCE peak is found for the 125 °C sample with a value of 19.9% (J – V measurement shown in Figure S1). The PCE increases from about 15.4% at 100 °C and decreases with increasing annealing temperature for temperatures >125 °C. This maximum value at 125 °C is close to the record PCE of 20.3% reported for single-junction solar cells with slot-die-coated THP absorbers.¹ The FF as well as the V_{oc} values exhibit an increase from 100 to 125 °C followed by a steady decrease for annealing temperatures ranging from 125 to 170 °C. The solar cells annealed at 125 °C exhibited maximum values of FF = 80% and V_{oc} = 1.23 V (not in the same solar cell). On the other hand, the median values of J_{sc} remain within the interval between about 19.5 and 20 mA/cm². Therefore, the PCE decrease visible between 125 and 170 °C is mainly due to decreases in FF and V_{oc} .

The irregular parameters of the 100 °C samples indicate insufficient crystallization at such low temperatures. This

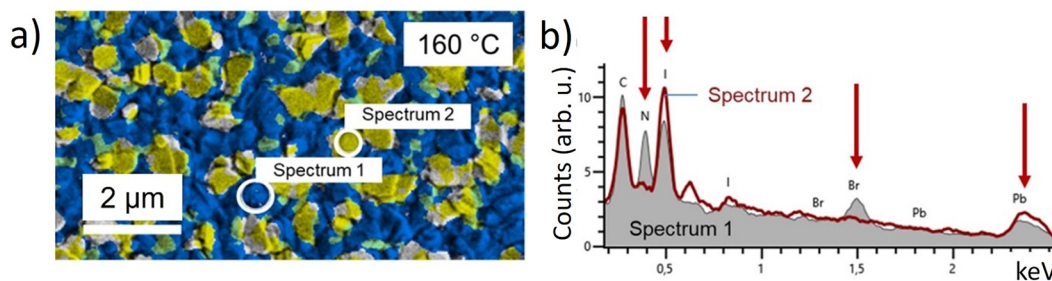


Figure 5. (a) Composite map superimposing the elemental distributions of I (yellow) and N (blue) obtained by EDX (I M and N K X-ray lines) to confirm the presence of PbI_2 phases. Two different and significantly varying regions in the EDX map were selected (white circles), and the corresponding EDX spectrum 1 (gray filled) and spectrum 2 (red line) extracted and depicted in part b. These spectra revealed that, compared with the THP matrix, the assumed PbI_2 precipitates are depleted in N and Br and enriched in Pb and I, as expected for PbI_2 .

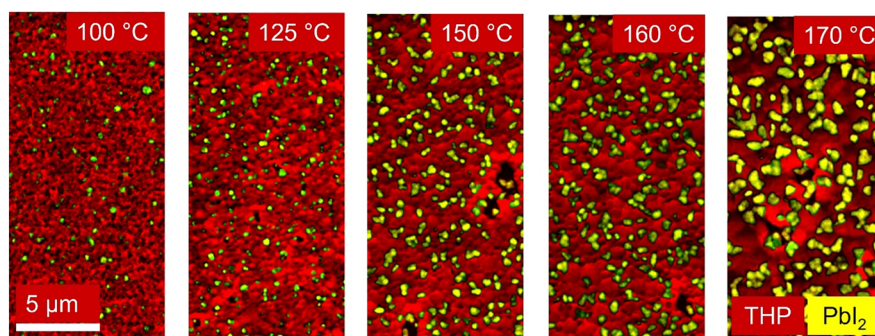


Figure 6. CL composite maps in plane view consisting of the 750 ± 50 nm band-pass filter signal corresponding to the THP luminescence (red) and the 500 ± 50 nm band-pass filter signal corresponding to PbI_2 (yellow).

assumption is further strengthened and discussed in the following results and discussions.

Microscopic Analyses of the THP Thin Films. For correlation of the solar-cell parameters and efficiencies with the THP thin-film properties on the submicron scale, various techniques in SEM were applied to THP/SAM/ITO/glass stacks. The SE images of all five samples (Figure 3) show contiguous THP thin films. The sizes of the crystallites increase with increasing annealing temperature, as was already reported for the 100, 150, and 170 °C samples in the previous study by Xu et al.⁷

While SE images are suitable for estimations of grain sizes, EBSD maps provide accurate grain-size and grain-orientation distributions. Figure 4a shows EBSD orientation maps in which different colors correspond to different crystal orientations. The black regions in the maps are those on which the EBSD patterns were not able to be indexed by the software; this may be due to shading via surface roughness and the 70° sample tilt during the measurement or due to grain sizes smaller than the EBSD detection limit.

To analyze the effect of surface roughness of the THP layers with PbI_2 secondary phases and its effect on the solar-cell performance, we first acquired cross-sectional SEM images (Figures S2 and S3). These images depict the film surface under a small viewing angle and do not exhibit any strong roughnesses. Moreover, it may be assumed that the film roughness affects the coverage of the C_{60} contact layer. However, cross-sectional SEM images and EDX measurements of the completed solar-cell stack (Figure S2) depict a continuous C_{60} layer. It should be noted that, in the present work, the C_{60} layer thickness was about 23 nm, and other publications reported that full coverage of the C_{60} layer can be achieved already at a thickness of 2.3 nm⁸ and that even an

ultrathin C_{60} film of about 1 nm thickness can still be functional in terms of efficient solar-cell operation.⁹

The THP thin films exhibit a preferred orientation perpendicular to the {101} crystal planes with no significant differences for the five different temperatures. The increase in the grain size with increasing annealing temperature is visible as well (Figure 4). The corresponding measured grain sizes are provided in Table S1.

From the EBSD data sets, also the phase distributions can be extracted (Figure 4b). Apparently, the thin films consist of the THP phase with fractions of the PbI_2 precipitates. With increasing annealing temperature, an increase in the area fraction of PbI_2 crystallites can be detected. The presence of PbI_2 was already discovered by Xu et al.⁷ and was unexpected because no excess in PbI_2 was provided during the THP thin-film synthesis. While this previous study provided first hints of an increasing amount of PbI_2 by XRD and grazing-incidence XRD, the electron microscopy analyses in the present work directly mapped the distributions of PbI_2 on the THP thin films.

For confirmation of the phase distributions obtained by EBSD, EDX measurements were applied (Figure 5). However, it was not possible to identify the PbI_2 precipitates unambiguously in the EDX elemental distribution maps. In these maps, regions were present that exhibited enhanced Pb and I signals, as expected for the PbI_2 precipitates. The differences in the Pb and I signals between the THP matrix and these regions were too small to be easily detectable in the maps. This fact, also given that rather low electron-beam energies of 3.5 keV lead to low information depths of the measurements, indicates that the extensions of the precipitates in the direction perpendicular to the substrate are very small, about 10–20 nm, which gives rise to the conclusion that the

PbI₂ precipitates are present at the surface as platelets. To highlight the compositional differences between the precipitates and the matrix, the N (blue) and I (yellow) signals are superimposed in Figure 5a. From the regions marked by white circles, EDX spectra were extracted from the THP matrix and the Pb-rich and I-rich regions (Figure 5b). From these two spectra, it is apparent that the precipitates are depleted in N and Br and enriched in Pb and I, as expected for PbI₂.

CL analyses were able to effectively map the PbI₂ phases on top of the THP thin films. The main CL peak energy of 1.69 eV (734 nm), expected for the THP phase (Figure S4), agrees well with PL measurements (Figure S5a), and measured peak energies of PbI₂ at 2.43 eV (511 nm) are in the expected range as well.¹ By the superimposition of monochromatic CL images acquired using band-pass filters of 750 ± 50 and 500 ± 50 nm, detailed false-color maps of the THP and PbI₂ phase distributions were obtained (Figure 6). These CL images reveal the area coverage of the PbI₂ precipitates on top of the THP thin films. The two phases were very distinguishable, which allowed for a quantification of the results employing image segmentation and further analyses of the PbI₂ coverage.

The cross-sectional CL image in Figure 7, in which once more the PbI₂ (yellow) and THP (red) phase distributions are

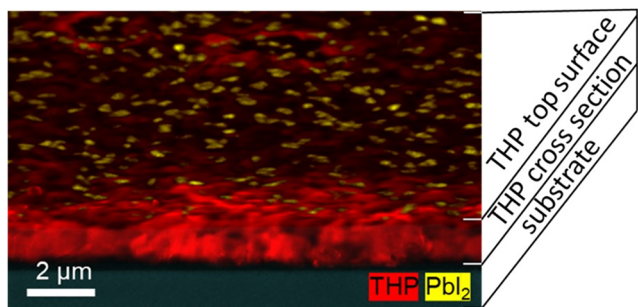


Figure 7. Cross-sectional CL composite map consisting of the 750 ± 50 nm band-pass filter signal including the THP luminescence (red) and the 500 ± 50 nm band-pass filter signal for PbI₂ (yellow).

depicted superimposed on the SEM image, shows the PbI₂ covered surface of the thin film without any PbI₂ precipitates detectable within the bulk of the THP thin film. This result confirms that PbI₂ precipitates form as platelets only on the film surface during the annealing process. If PbI₂ precipitates were existent in considerable amounts in the bulk, it would be easily revealed by microscopic investigations in the cross section, as shown by other reports.¹⁰ However, no PbI₂ was detected in the THP bulk by EDX measurements on cross-sectional specimens prepared from solar-cell stacks (Figure S2).

Influence of PbI₂ Coverage on FF and R_s. A common reason for low FF values is the high series resistance R_s of the solar cell. The increasing area fraction of PbI₂ can increase R_s, which strongly influences the FF.¹¹ The shunt resistance was analyzed as well; however, the determined median values of 0.6–2.4 kΩ·cm² did not indicate any shunting or other deterioration of the photovoltaic performance (Figure S6b).

Figure 8a shows the PbI₂ thin-film coverage plotted as a function of the median series resistance of the measured solar cells. The data of the coverage were extracted from the CL images by image segmentation, while the R_s data originated from the measured J–V curves of the solar cells. The

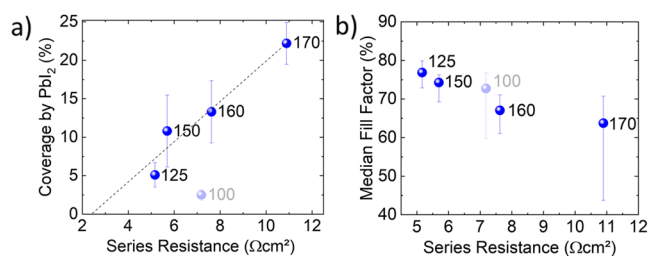


Figure 8. (a) Estimated PbI₂ coverage as a function of the median series resistance R_s with a guide for the eyes (dashed line) showing a theoretical PbI₂-free R_s of 2.5 Ω·cm² at the x intercept and (b) median FF as a function of the median R_s. Data points are labeled with their corresponding annealing temperatures in degrees Celsius. The 100 °C line is illustrated in light gray to mark it as an outlier.

viewgraph in Figure 8a reveals a quasilinear correlation between PbI₂ and the median R_s for all temperatures except for 100 °C. This linear relationship agrees with an assumption of a decrease in the conductor cross section with increasing PbI₂ coverage. The coverage is about 3% at 100 °C and reaches about 22% at 170 °C. R_s exhibits a higher value of 7 Ω·cm² at 100 °C, decreases to its minimum of 5 Ω·cm² at 125 °C, and increases to 11 Ω·cm² at 170 °C. To check the R_s values for consistency, FF and R_s were plotted (Figure 8b) and should follow the approximately linear behavior as described by Green's empirical expression:¹²

$$FF = FF_0 \left(1 - 1.1 R_s \frac{J_{sc}}{V_{oc}} \right) + \frac{\left(R_s \frac{J_{sc}}{V_{oc}} \right)^2}{5.4} \quad (1)$$

where FF₀ corresponds to a fill factor without the influence of R_s. For large characteristic resistances R_{ch} = $\frac{V_{oc}}{J_{sc}}$ compared with R_s, it can be approximately described as linear, as shown in Figure 8b. The 100 °C sample and its median R_s stand out due to its insufficient film crystallization, which makes it a poor semiconductor without the influence of PbI₂ secondary phases.

Influence of PbI₂ on V_{oc}. V_{oc} decreases as well with an increase in the annealing temperature (Figure 2b). Figure 9a indicates a linear correlation between the thin-film coverage by PbI₂ and a decrease in the median V_{oc} values. The 100 °C data point is an outlier again. The linear regression reveals a potential PbI₂-free median V_{oc} of about 1.25 V. Describing the exact correlation between recombination and the amount of

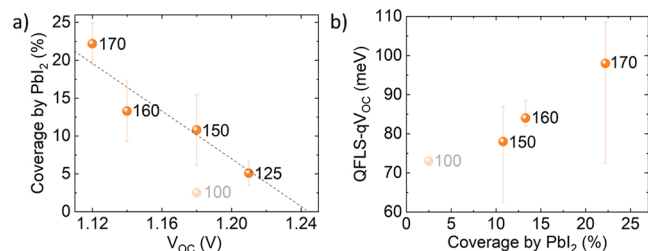


Figure 9. (a) Estimated PbI₂ coverage as a function of the median V_{oc}. The dashed line corresponds to a guide for the eye, pointing to a hypothetical V_{oc} without any PbI₂ coverage. (b) Mismatch between QFLS and median V_{oc} as a function of the PbI₂ coverage for the annealing temperatures 100, 150, 160, and 170 °C (data for 125 °C were not available), indicating increasing recombination losses with increasing amounts of PbI₂.

PbI₂ on the surface of the THP thin film is more complex than referring only to the correlation between R_s and PbI₂. This is because PbI₂ may have passivating properties^{13,14} in appropriate amounts and at corresponding locations, and complete removal may potentially reduce surface passivation or even generate new recombination centers. Additionally, the band-gap energy decreases with increasing annealing temperature, as indicated by mean measured PL peak energies ranging from 1.67 to 1.65 eV (Figure S5). This result can be attributed to a loss of chlorine, which leads to a further decrease of V_{oc}. Such an issue is independent of PbI₂ and difficult to avoid but plays only a minor role in the temperature-dependent V_{oc} decrease.

Figure 9b shows the mismatch between quasi-Fermi-level splitting (QFLS) and the measured V_{oc}, indicating increasing recombination losses with increasing THP thin-film coverage by PbI₂ platelets. The effective lifetimes obtained from time-resolved photoluminescence (TRPL) measurements (Figure S7) on the THP thin films without an electron-transport layer (ETL; Table S2) are about the same order of magnitude (about 300 ± 100 ns) for the entire temperature range. Thus, we neglected any strong contributions of the THP bulk properties to the performance losses found with the annealing temperature. Rather, elevated recombination rates at the THP/C₆₀ interface in connection with the PbI₂ platelets must be considered.

Formation of PbI₂ and Its Effects on the Solar Cell Performance. The formation of PbI₂ in slot-die-coated THP films is not a result of differences in the chemical compositions already in the inks but of compositional changes occurring in the fabricated THP films after the annealing process. The elevated annealing temperatures of 100–170 °C, compared with lower temperatures in antisolvent-quenched spin-coating film depositions, lead to an increased evaporation rate of organic compounds in the THP ink during the annealing step and finally to a collapse of the ABX₃ perovskite structure.

In the past, when investigating the synthesis of the mixed-halide perovskite MAPb_{3-x}Cl_x was very popular, a material that in most cases did not contain chloride in detectable amounts, it was found that annealing temperatures above 100 °C led to significant losses of MAI.^{15,16} The same can also be assumed for FACl in THPs containing FA and Cl. A study conducted by Song et al.¹⁷ showed how volatile compounds such as FACl and MAI influence the stoichiometric ratios in gas-quenched (without the application of antisolvents) perovskite absorber layers by different annealing parameters. It is assumed that FACl/MAI losses lead to Pb-rich surfaces, eventually resulting in the formation of PbI₂ on the film surfaces. While Song et al.¹⁷ correlated the thin-film stoichiometry with the device performances, these authors did not link the impaired device performances and stabilities with the amount of PbI₂. Guo et al.¹⁸ explained the presence of PbI₂ at the film surface by the migration of excess PbI₂ to material interfaces.

An indication for chloride losses in the THP films studied in the present work was found by means of PL. The PL peak energies (Figure S5a) decreased from 1.67 to 1.65 eV for annealing temperatures increasing from 150 to 170 °C. However, this difference is not sufficient to explain the performance losses of the corresponding solar cells.

Several authors reported that an increase of PbI₂ on the surface of perovskite thin films can be beneficial for the solar-cell performance,^{13,14,19–22} due to passivation of the interfaces^{13,14} but also due to important influences on the

thin-film formation and crystallization.²² In this study, the detrimental effects of PbI₂ clearly predominate. One reason for this fact is that the solar-cell structure in the present work differs from most of these reports. In studies and publications dealing with regular solar-cell structures, PbI₂ was generally situated between the halide–perovskite absorber layer and hole-transport layer.

For integration of the THP solar cell as the top cell in a tandem device,²³ the “inverted” perovskite solar-cell structure was used in the present work. In this inverted structure, PbI₂ is located at the interface between THP and the ETL, as shown in Figure 10a. The detrimental effect of PbI₂ in this structure is

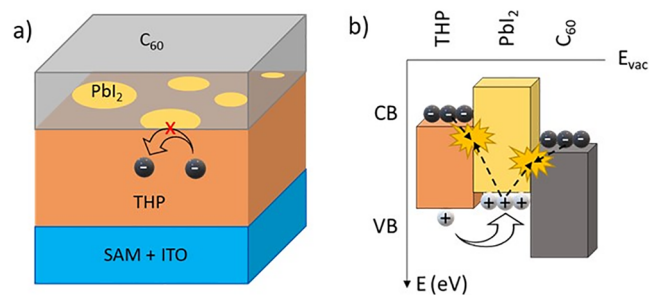


Figure 10. (a) Schematic of PbI₂ platelets situated at the THP/C₆₀ interface in the ITO/SAM/THP/C₆₀ stack, a part of an inverted THP solar cell, and (b) schematic band diagram depicting the detrimental effects of PbI₂ at the THP/C₆₀ interface on the charge-carrier transport and recombination processes.

a consequence of its elevated conduction band edge compared with those of perovskite compounds usually applied in solar cells. This fact explains why PbI₂ may block photogenerated electrons from THP and inhibits transfer to the ETL.^{24–27} Nevertheless, even the alignment of the perovskite–PbI₂ heterojunction is a matter of debate.²² We assume an electron-blocking behavior by forming a type 1 alignment²⁶ or type 2 alignment (Figure 10) with hole-injecting properties.²⁵ Both alignment types are detrimental in inverse THP solar-cell structures.

There are indeed reports claiming beneficial effects even at the absorber–ETL interface; however, they are about the passivation of TiO₂, which was not applied in the present work.¹³ Instead, we integrated LiF-passivated C₆₀ as a selective ETL. The interface between this ETL and PbI₂ is not yet well investigated. Regarding long-term stability, PbI₂ is widely seen as a degradation accelerator and reduces the device stability.^{28–31} We have not analyzed the long-term stability, but we assume a stability-harming effect of PbI₂ in our samples.

It should be noted that the detrimental effect of PbI₂ is not an issue exclusively in THP solar cells. It can be generalized to all perovskite-type solar cells with inverted cell structure, containing an absorber with a conduction band edge of several 100 meV lower than that of PbI₂²⁴ and with a suitable amount of PbI₂ present at the absorber–ETL interface.

Correlation of the Microstructure and Solar-Cell Performances. The experimental results revealed the 100 °C sample as an outlier in the measurements of the solar-cell parameters. Treating it as an outlier is based on the results and conclusions of XRD (Figure S8) and EBSD measurements (Figure 4). In the XRD patterns, the (100) Bragg diffraction peak of the THP at around 14.2° of the 100 °C sample exhibits the largest full width at half-maximum compared with those of

the other samples. Additionally, the large fraction of non-indexed areas in EBSD mappings are an indication for regions with grain sizes below the detection limit of the EBSD system. Such small grain sizes correspond to high grain-boundary densities with the result of lower charge-carrier mobilities and increased recombination losses. Thin-film formation at lower temperatures, such as 100 °C, is usually promoted and enhanced by the application of antisolvents in spin coating, but for large-area depositions and in future roll-to-roll processes, antisolvents cannot be sufficiently supplied.^{7,32} Annealing temperatures of 100 °C are not sufficient to form grains of suitable sizes, and even leftovers of intermediate phases could be speculated; therefore, the 100 °C samples are excluded from following analyses and discussions. The inability to use antisolvents makes the annealing temperature one of the most important parameters for perovskite thin-film crystallization in slot-die coating. We consider an annealing temperature of 125 °C as the lower limit, where a desired crystallization can be expected without the application of antisolvents.

The goal of the correlation between the THP thin-film microstructure measured by techniques of electron microscopy and the solar-cell performance parameter is to understand the mechanisms behind the evolution of solar-cell parameters with increasing annealing temperatures. The electron microscopy analyses revealed two main trends: temperature-dependent grain sizes and temperature-dependent area fractions of PbI₂ platelets on the surfaces of the THP thin films. Furthermore, the solar-cell parameters exhibit the following trends with increasing annealing temperature: no significant change in the J_{sc} values and decreases in V_{oc} , FF, and (as a result of these trends) PCE.

The measured increase in the grain size is considered to be a beneficial influence on the solar-cell performance because grain boundaries are commonly known as locations of increased nonradiative recombination.³³ Grain boundaries can scatter charge carriers and, finally, decrease their mobility. Larger grain sizes are equivalent to a lower grain-boundary density in the bulk material, and as a result, the bulk recombination decreases. Lower recombination rates and high charge-carrier mobility lead to a higher amount of collectable charge carriers and finally should increase J_{sc} , which we did not find. The same positive effects are expected for the V_{oc} value because it is a parameter connected to recombination processes in solar cells. An increase in recombination losses with increasing annealing temperature can be regarded as the main reason for low V_{oc} values. Therefore, another presumably PbI₂-related mechanism rules the recombination processes, opposing the beneficial effect of increasing grain sizes.

Analyses of the PL measurements provided values for QFLS in the THP thin films. Such QFLS values represent the upper limit of qV_{oc} . A mismatch between QFLS and qV_{oc} indicates losses due to recombination processes, which seem to increase strongly with increasing annealing temperature (Figure 9b). The reason for the increasing recombination rates might be the opening of new recombination pathways by PbI₂ (Figure 10b). Holes can enter PbI₂ and potentially recombine with blocked electrons in the THP or electrons in the C₆₀ ETL.

The blocking of electrons by PbI₂ explains the increase in R_s with increasing PbI₂ coverage. The linear correlation between the PbI₂ coverage and R_s allows a linear approximation of a hypothetical R_s of PbI₂-free solar cells (Figure 8). As a result, a PbI₂-free R_s of 2.5 Ω·cm² was determined. The measured

values for FF and PCE in Figure 2 can be recalculated with the hypothetical PbI₂-free R_s using Green's equation (eq 1) to model the potential of complete PbI₂ removal.

The simulated effect of PbI₂ removal is shown in Figure 11. It reveals an overall increase of FF (Figure 11a), median values

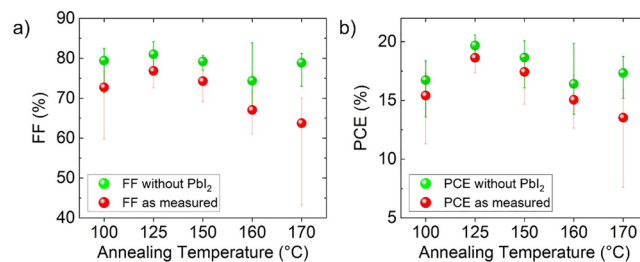


Figure 11. Simulated data of (a) FF and (b) PCE with the subtracted influence of PbI₂ by recalculating FF and PCE using eq 1 with an approximated median R_s for a 0% PbI₂ thin-film coverage of 2.5 Ω·cm². The median gain in the PCE was calculated to be about 1–2%. For comparison, the measured median values are included in red.

exceeding 80%, and median PCEs reaching almost 20% (Figure 11b), as well as a flattening of the decreasing trend with increasing annealing temperatures. The comparison with measured mean PCE values exhibits that all, but especially the 170 °C sample, would benefit from such a removal. The potential gain of PbI₂ removal regarding the PCE is at least 1%. In a similar way, a PbI₂-free V_{oc} of more than 1.24 V can be determined and would double the PCE gain to more than 2%. Attempts to remove PbI₂ have already been done by polishing or chemical washout,^{34,35} but complete removal has not been achieved yet.

Notably, the presented model requires the entire removal of PbI₂, which is not easily done. Such a removal may even lead to a lack of PbI₂ and the potential opening of new recombination pathways because the presence of PbI₂ has been reported to enhance passivation.^{13,14} Another potential effect missing in the present model is a presumable increase in J_{sc} with increasing annealing temperature due to the increase in the grain size, reducing grain-boundary recombination and due to enhanced collection by reducing the PbI₂ interface recombination.

CONCLUSION

The present study showed that the PCE of solar cells with slot-die-coated THP absorbers is limited by increased area fractions of PbI₂ precipitates on the THP thin-film surface with increased annealing temperature. By means of correlative electron microscopy, we demonstrated that, while a temperature of 100 °C is not sufficient without the application of antisolvents, the samples annealed at temperatures above 125 °C revealed a correlation between the PbI₂ coverage and photovoltaic parameters. The stronger coverage of the THP thin-film surface by PbI₂ precipitates causes a significant increase in the series resistance R_s of the corresponding solar cells, which again is responsible for the decreasing FF values. Moreover, the PbI₂ precipitates give rise to recombination pathways at the interfaces, leading to V_{oc} losses. These detrimental effects of PbI₂ are even more effective in inverted perovskite solar-cell structures due to its accumulation at the THP–ETL interface.

We estimated that complete removal of PbI_2 by chemical polishing or washing will lead to an absolute PCE gain of at least 1%. This removal would prevent higher series resistances and recombination pathways induced by the PbI_2 precipitates and allow enhanced device performance at higher annealing temperatures via larger average grain sizes.

■ ASSOCIATED CONTENT

SI Supporting Information

The Supporting Information is available free of charge at <https://pubs.acs.org/doi/10.1021/acsami.3c07692>.

Experimental details of materials synthesis and sample preparation and additional results, tables of EBSD data and TRPL results, and figures of CL spectra, PL data, XRD data, series and shunt resistance data, EDX data of solar-cell cross sections, and SE images of cross sections (PDF)

■ AUTHOR INFORMATION

Corresponding Authors

Dan R. Wargulski – Helmholtz- Zentrum Berlin für Materialien und Energie GmbH, 14109 Berlin, Germany; orcid.org/0000-0002-3752-6466; Email: dan.wargulski@helmholtz-berlin.de

Daniel Abou-Ras – Helmholtz- Zentrum Berlin für Materialien und Energie GmbH, 14109 Berlin, Germany; orcid.org/0000-0003-3063-922X; Email: daniel.abou-ras@helmholtz-berlin.de

Authors

Ke Xu – Helmholtz- Zentrum Berlin für Materialien und Energie GmbH, 14109 Berlin, Germany; orcid.org/0000-0002-1113-1095

Hannes Hempel – Helmholtz- Zentrum Berlin für Materialien und Energie GmbH, 14109 Berlin, Germany

Marion A. Flatken – Helmholtz- Zentrum Berlin für Materialien und Energie GmbH, 14109 Berlin, Germany

Steve Albrecht – Helmholtz- Zentrum Berlin für Materialien und Energie GmbH, 14109 Berlin, Germany; Faculty of Electrical Engineering and Computer Science, Technische Universität Berlin, 10587 Berlin, Germany; orcid.org/0000-0001-9962-9535

Complete contact information is available at: <https://pubs.acs.org/10.1021/acsami.3c07692>

Author Contributions

D.R.W. and D.A.-R. planned the electron microscopy experiments and analyzed and interpreted the results. K.X. and S.A. defined the problem and delivered the aim of the study. D.R.W. conducted the electron microscopy experiments (SE imaging, EDX, EBSD, and CL measurements) and prepared the figures. K.X. fabricated the samples and conducted the solar-cell characterization (determination of PCE, FF, V_{oc} , J_{sc} , R_s , and R_p). H.H. conducted the PL and TRPL experiments and M.A.F. the XRD measurements. D.A.-R. and S.A. supervised the work. All authors contributed to data interpretation and manuscript writing. All authors have given approval to the final version of the manuscript.

Notes

The authors declare no competing financial interest.

■ ACKNOWLEDGMENTS

We thank Sinju Thomas and Dr. Klaus Schwarzburg from Helmholtz-Zentrum Berlin (HZB) for their scientific and technical support and assistance on the scanning electron microscopes, Ulrike Bloeck (HZB) for help with the sample preparation, and Prof. Susan Schorr (HZB) and Prof. Michael Lehmann (Technische Universität Berlin) for scientific advice. We highly appreciate the support of René Schwiddessen (HZB), who conducted additional XRD measurements. We further acknowledge the international research school HIRSCORE (HIRS-008) and the graduate school HyPerCells for support as well as the Helmholtz Innovation Lab HySPRINT. In addition, we acknowledge the Federal Ministry for Economic Affairs and Energy (BMWi) for funding of the project PrEsto (Grant 03EE1086C).

■ REFERENCES

- (1) Xu, J.; Boyd, C. C.; Yu, Z. J.; Palmstrom, A. F.; Witter, D. J.; Larson, B. W.; France, R. M.; Werner, J.; Harvey, S. P.; Wolf, E. J.; Weigand, W.; Manzoor, S.; van Hest, M. F. A. M.; Berry, J. J.; Luther, J. M.; Holman, Z. C.; McGehee, M. D. Triple-Halide Wide-Band Gap Perovskites with Suppressed Phase Segregation for Efficient Tandems. *Science* (80-). **2020**, *367* (6482), 1097–1104.
- (2) Nie, T.; Fang, Z.; Ren, X.; Duan, Y.; Liu, S. Recent Advances in Wide-Bandgap Organic-Inorganic Halide Perovskite Solar Cells and Tandem Application. *Nano-Micro Lett.* **2023**, *15* (1), 1–44.
- (3) Jošt, M.; Köhnen, E.; Morales-Vilches, A. B.; Lipovšek, B.; Jäger, K.; Macco, B.; Al-Ashouri, A.; Krč, J.; Korte, L.; Rech, B.; Schlattmann, R.; Topič, M.; Stannowski, B.; Albrecht, S. Textured Interfaces in Monolithic Perovskite/Silicon Tandem Solar Cells: Advanced Light Management for Improved Efficiency and Energy Yield. *Energy Environ. Sci.* **2018**, *11* (12), 3511–3523.
- (4) Hoke, E. T.; Slotcavage, D. J.; Dohner, E. R.; Bowring, A. R.; Karunadasa, H. I.; McGehee, M. D. Reversible Photo-Induced Trap Formation in Mixed-Halide Hybrid Perovskites for Photovoltaics. *Chem. Sci.* **2015**, *6* (1), 613–617.
- (5) Unger, E. L.; Kegelman, L.; Suchan, K.; Sörell, D.; Korte, L.; Albrecht, S. Roadmap and Roadblocks for the Band Gap Tunability of Metal Halide Perovskites. *J. Mater. Chem. A* **2017**, *5* (23), 11401–11409.
- (6) NREL. NREL Chart (July 2023), <https://www.nrel.gov/pv/cell-efficiency.html>.
- (7) Xu, K.; Al-Ashouri, A.; Peng, Z. W.; Köhnen, E.; Hempel, H.; Akhundova, F.; Marquez, J. A.; Tockhorn, P.; Shargaieva, O.; Ruske, F.; Zhang, J.; Dagar, J.; Stannowski, B.; Unold, T.; Abou-Ras, D.; Unger, E.; Korte, L.; Albrecht, S. Slot-Die Coated Triple-Halide Perovskites for Efficient and Scalable Perovskite/Silicon Tandem Solar Cells. *ACS Energy Lett.* **2022**, *7* (10), 3600–3611.
- (8) Warby, J.; Zu, F.; Zeiske, S.; Gutierrez-Partida, E.; Frohloff, L.; Kahmann, S.; Frohna, K.; Mosconi, E.; Radicchi, E.; Lang, F.; Shah, S.; Peña-Camargo, F.; Hempel, H.; Unold, T.; Koch, N.; Armin, A.; De Angelis, F.; Stranks, S. D.; Neher, D.; Stolterfoht, M. Under-Performance Limiting Interfacial Recombination in Pin Perovskite Solar Cells. *Adv. Energy Mater.* **2022**, *12* (12), 2103567.
- (9) Liu, D.; Wang, Q.; Traverse, C. J.; Yang, C.; Young, M.; Kuttipillai, P. S.; Lunt, S. Y.; Hamann, T. W.; Lunt, R. R. Impact of Ultrathin C60 on Perovskite Photovoltaic Devices. *ACS Nano* **2018**, *12* (1), 876–883.
- (10) Yang, X.; Luo, D.; Xiang, Y.; Zhao, L.; Anaya, M.; Shen, Y.; Wu, J.; Yang, W.; Chiang, Y. H.; Tu, Y.; Su, R.; Hu, Q.; Yu, H.; Shao, G.; Huang, W.; Russell, T. P.; Gong, Q.; Stranks, S. D.; Zhang, W.; Zhu, R. Buried Interfaces in Halide Perovskite Photovoltaics. *Adv. Mater.* **2021**, *33* (7), 2006435.
- (11) Pysch, D.; Mette, A.; Glunz, S. W. A Review and Comparison of Different Methods to Determine the Series Resistance of Solar Cells. *Sol. Energy Mater. Sol. Cells* **2007**, *91* (18), 1698–1706.

- (12) Green, M. A. Accuracy of Analytical Expressions for Solar Cell Fill Factors. *Sol. Cells* **1982**, *7* (3), 337–340.
- (13) Nakayashiki, S.; Daisuke, H.; Ogomi, Y.; Hayase, S. Interface Structure between Titania and Perovskite Materials Observed by Quartz Crystal Microbalance System. *J. Photon. Energy* **2015**, *5* (1), 057410.
- (14) Chen, Y.; Meng, Q.; Xiao, Y.; Zhang, X.; Sun, J.; Han, C. B.; Gao, H.; Zhang, Y.; Lu, Y.; Yan, H. Mechanism of PbI₂ in Situ Passivated Perovskite Films for Enhancing the Performance of Perovskite Solar Cells. *ACS Appl. Mater. Interfaces* **2019**, *11* (47), 44101–44108.
- (15) Chae, J.; Dong, Q.; Huang, J.; Centrone, A. Chloride Incorporation Process in CH₃NH₃PbI_{3-x}Cl_x Perovskites via Nano-scale Bandgap Maps. *Nano Lett.* **2015**, *15*, 8114.
- (16) Zhao, Y.; Zhu, K. Efficient Planar Perovskite Solar Cells Based on 1.8 eV Band Gap CH₃NH₃PbI₂Br Nanosheets via Thermal Decomposition. *J. Am. Chem. Soc.* **2014**, *136*, 12241.
- (17) Song, W.; Zhang, X.; Lammar, S.; Qiu, W.; Kuang, Y.; Ruttens, B.; D'Haen, J.; Vaesen, I.; Conard, T.; Abdurraheem, Y.; Aernouts, T.; Zhan, Y.; Poortmans, J. Critical Role of Perovskite Film Stoichiometry in Determining Solar Cell Operational Stability: A Study on the Effects of Volatile A-Cation Additives. *ACS Appl. Mater. Interfaces* **2022**, *14*, 27922.
- (18) Guo, R.; Han, D.; Chen, W.; Dai, L.; Ji, K.; Xiong, Q.; Li, S.; Reb, L. K.; Scheel, M. A.; Pratap, S.; Li, N.; Yin, S.; Xiao, T.; Liang, S.; Oechsle, A. L.; Weindl, C. L.; Schwartzkopf, M.; Ebert, H.; Gao, P.; Wang, K.; Yuan, M.; Greenham, N. C.; Stranks, S. D.; Roth, S. V.; Friend, R. H.; Müller-Buschbaum, P. Degradation Mechanisms of Perovskite Solar Cells under Vacuum and One Atmosphere of Nitrogen. *Nat. Energy* **2021**, *6* (10), 977–986.
- (19) Park, B.-w.; Kedem, N.; Kulbak, M.; Lee, D. Y.; Yang, W. S.; Jeon, N. J.; Seo, J.; Kim, G.; Kim, K. J.; Shin, T. J.; Hodes, G.; Cahen, D.; Seok, S. Il. Understanding How Excess Lead Iodide Precursor Improves Halide Perovskite Solar Cell Performance. *Nat. Commun.* **2018**, *9* (1). DOI: 10.1038/s41467-018-05583-w.
- (20) Wang, H.; Wang, Z.; Yang, Z.; Xu, Y.; Ding, Y.; Tan, L.; Yi, C.; Zhang, Z.; Meng, K.; Chen, G.; Zhao, Y.; Luo, Y.; Zhang, X.; Hagfeldt, A.; Luo, J. Ligand-Modulated Excess PbI₂ Nanosheets for Highly Efficient and Stable Perovskite Solar Cells. *Adv. Mater.* **2020**, *32* (21), 2000865.
- (21) Cao, D. H.; Stoumpos, C. C.; Malliakas, C. D.; Katz, M. J.; Farha, O. K.; Hupp, J. T.; Kanatzidis, M. G. Remnant PbI₂, an Unforeseen Necessity in High-Efficiency Hybrid Perovskite-Based Solar Cells? *Cit. APL Mater.* **2014**, *2*, 91101.
- (22) Jacobsson, T. J.; Correa-Baena, J. P.; Halvani Anaraki, E.; Philippe, B.; Stranks, S. D.; Bouduban, M. E. F.; Tress, W.; Schenk, K.; Teuscher, J.; Moser, J. E.; Rensmo, H.; Hagfeldt, A. Unreacted PbI₂ as a Double-Edged Sword for Enhancing the Performance of Perovskite Solar Cells. *J. Am. Chem. Soc.* **2016**, *138* (32), 10331–10343.
- (23) Köhnen, E.; Jošt, M.; Morales-Vilches, A. B.; Tockhorn, P.; Al-Ashouri, A.; Macco, B.; Kegelmann, L.; Korte, L.; Rech, B.; Schlattmann, R.; Stannowski, B.; Albrecht, S. Highly Efficient Monolithic Perovskite Silicon Tandem Solar Cells: Analyzing the Influence of Current Mismatch on Device Performance. *Sustain. Energy Fuels* **2019**, *3* (8), 1995–2005.
- (24) Caputo, M.; Cefarin, N.; Radivo, A.; Demitri, N.; Gigli, L.; Plaisier, J. R.; Panighel, M.; Di Santo, G.; Moretti, S.; Giglia, A.; Polentarutti, M.; De Angelis, F.; Mosconi, E.; Umari, P.; Tormen, M.; Goldoni, A. Electronic Structure of MAPbI₃ and MAPbCl₃: Importance of Band Alignment. *Sci. Reports* **2019**, *9* (1), 1–11.
- (25) Calloni, A.; Abate, A.; Bussetti, G.; Berti, G.; Yivlialin, R.; Ciccacci, F.; Duò, L. Stability of Organic Cations in Solution-Processed CH₃NH₃PbI₃ Perovskites: Formation of Modified Surface Layers. *J. Phys. Chem. C* **2015**, *119* (37), 21329–21335.
- (26) Chen, Q.; Zhou, H.; Song, T. B.; Luo, S.; Hong, Z.; Duan, H. S.; Dou, L.; Liu, Y.; Yang, Y. Controllable Self-Induced Passivation of Hybrid Lead Iodide Perovskites toward High Performance Solar Cells. *Nano Lett.* **2014**, *14* (7), 4158–4163.
- (27) Xu, H.; Wu, Y.; Cui, J.; Ni, C.; Xu, F.; Cai, J.; Hong, F.; Fang, Z.; Wang, W.; Zhu, J.; Wang, L.; Xu, R.; Xu, F. Formation and Evolution of the Unexpected PbI₂ Phase at the Interface during the Growth of Evaporated Perovskite Films †. *Phys. Chem. Chem. Phys.* **2016**, *18*, 18607.
- (28) Kapoor, V.; Bashir, A.; Haur, L. J.; Bruno, A.; Shukla, S.; Priyadarshi, A.; Mathews, N.; Mhaisalkar, S. Effect of Excess PbI₂ in Fully Printable Carbon-Based Perovskite Solar Cells. *Energy Technol.* **2017**, *5* (10), 1880–1886.
- (29) Liu, F.; Dong, Q.; Wong, M. K.; Djurišić, A. B.; Ng, A.; Ren, Z.; Shen, Q.; Surya, C.; Chan, W. K.; Wang, J.; Ng, A. M. C.; Liao, C.; Li, H.; Shih, K.; Wei, C.; Su, H.; Dai, J. Is Excess PbI₂ Beneficial for Perovskite Solar Cell Performance? *Adv. Energy Mater.* **2016**, *6* (7), 1502206.
- (30) Gujar, T. P.; Unger, T.; Schönleber, A.; Fried, M.; Panzer, F.; Van Smaalen, S.; Köhler, A.; Thelakkat, M. The Role of PbI₂ in CH₃NH₃PbI₃ Perovskite Stability, Solar Cell Parameters and Device Degradation †. *Phys. Chem. Chem. Phys.* **2018**, *20*, 605.
- (31) Tumen-Ulzii, G.; Qin, C.; Klotz, D.; Leyden, M. R.; Wang, P.; Auffray, M.; Fujihara, T.; Matsushima, T.; Lee, J. W.; Lee, S. J.; Yang, Y.; Adachi, C. Detrimental Effect of Unreacted PbI₂ on the Long-Term Stability of Perovskite Solar Cells. *Adv. Mater.* **2020**, *32* (16), 1905035.
- (32) Shargaieva, O.; Näsström, H.; Li, J.; Többsen, D. M.; Unger, E. L. Temperature-Dependent Crystallization Mechanisms of Methylammonium Lead Iodide Perovskite From Different Solvents. *Front. Energy Res.* **2021**. DOI: 10.3389/feenrg.2021.749604.
- (33) Kim, H. Do; Ohkita, H.; Benten, H.; Ito, S. Photovoltaic Performance of Perovskite Solar Cells with Different Grain Sizes. *Adv. Mater.* **2016**, *28* (5), 917–922.
- (34) Zhao, L.; Li, Q.; Hou, C.-H.; Li, S.; Yang, X.; Wu, J.; Zhang, S.; Hu, Q.; Wang, Y.; Zhang, Y.; Jiang, Y.; Jia, S.; Shyue, J.-J.; Russell, T. P.; Gong, Q.; Hu, X.; Zhu, R. Chemical Polishing of Perovskite Surface Enhances Photovoltaic Performances. *J. Am. Chem. Soc.* **2022**, *144*, 1700.
- (35) Hu, Z.; An, Q.; Xiang, H.; Aigouy, L.; Sun, B.; Vaynzof, Y.; Chen, Z. Enhancing the Efficiency and Stability of Triple-Cation Perovskite Solar Cells by Eliminating Excess PbI₂ from the Perovskite/Hole Transport Layer Interface. *ACS Appl. Mater. Interfaces* **2020**, *12* (49), 54824–54832.